

www.acsami.org Research Article

# Structural Formation and Pore Control of Freeze-Cast Directional Graphene Aerogel (DGA)

Mian U. Saeed,\* Yu-Kai Weng, Mohammad Bahzad, Seungha Shin, Doug S. Aaron, and Kenneth D. Kihm\*



Cite This: ACS Appl. Mater. Interfaces 2024, 16, 425-434

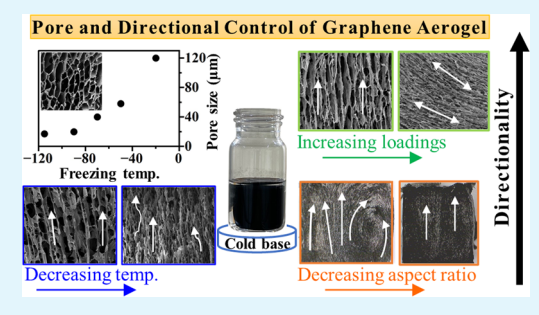


ACCESS

III Metrics & More

Article Recommendations

ABSTRACT: Directional graphene aerogels (DGAs) are proposed as electrode materials to alleviate ionic and mass transport issues in organic redox flow batteries (ORFBs). DGAs with high pore directionality would provide low resistance channels for effective ionic charge and liquid electrolyte transport in these devices. DGAs' porous and directional characteristics can be controlled by the growth of ice crystals during freeze casting, which is influenced by the self-diffusivity of water, phase change driving forces, water—ice graphene interactions, and convection in the water—graphene media. It is found that mass transport-related properties of DGAs, including pore size and directionality, show a significant dependence on freezing temperature, graphene oxide (GO) loadings, and synthesis vessel diameter-to-height ratio (D/H). For



the freezing temperature change from -20 to -115 °C, the average pore size progressively decreased from 120 to 20  $\mu$ m, and the pore directionality transitioned from lamellar to ill-defined structures. When GO loadings were increased from 2 to 10 mg/mL at a fixed freezing temperature, pore size reduction was observed with less defined directionality. Furthermore, the pore directionality diminished with an increased width-to-height aspect ratio of DGA samples due to the buoyancy-driven convective circulation, which interfered with the directional ice/pore growth. Understanding the comprehensive effects of these mechanisms enables the controlled growth of ice crystals, leading to graphene aerogels with highly directional microstructures.

KEYWORDS: directional graphene aerogel, freeze casting, self-diffusivity, phase change force, water-graphene interaction

#### 1. INTRODUCTION

**1.1. Graphene Aerogels (GAs).** Three-dimensional, conductive, porous architectures of graphene, i.e., graphene aerogels (GAs), have been increasingly implemented in a variety of fields such as biotechnology, photovoltaics, catalysis, and energy conversion, and environment. They offer a combination of functional properties, including low density, high active material content, high surface area, and a porous network, which are essential properties for facilitating numerous physiochemical phenomena critical to a range of applications. For example, the adsorption of CO<sub>2</sub> is improved with GAs, which is attributed to GA's high surface area.

The properties of GAs also make them promising electrode materials for battery applications, especially in flow batteries. Electrodes in battery systems are crucial, as they host electrochemical reactions, distribute the electroactive species to reaction regions, and conduct electrons and heat. However, electrode functions suffer from inefficiencies, giving rise to various overpotentials (kinetic, ohmic, and concentration) that ultimately limit battery electrochemical performance. In essence, major limitations in battery performance arise from the electrode properties.

1.2. Consideration of GAs for Organic Redox Flow Battery (ORFB) Electrodes. One proposed application for GAs is the implementation as electrodes for organic redox flow batteries (ORFBs), which utilize organic electroactive materials and are an emerging class of redox flow batteries (RFBs). 11,12 In contrast to aqueous RFBs, e.g., all-vanadium (VRFBs)<sup>13,14</sup> and zinc-bromine,<sup>15</sup> ORFBs offer wider voltage windows<sup>16</sup> and, higher energy densities<sup>17</sup> with competitive system costs, 18 making them promising RFB technology for long-duration energy storage. However, ORFBs are frequently limited by relatively poor mass and ionic transport, 12,19-21 leading to large concentration overpotentials. It is noteworthy to mention that all types of RFBs have mass transport limitations, but these limitations are more significant in organic electrolyte systems, as substantially higher viscous organic fluid flows are encountered in the electrodes. This mass transport

Received: July 26, 2023 Revised: December 11, 2023

Accepted: December 11, 2023

Published: December 20, 2023





limitation is recognized to be among the key issues to be addressed for these organic electrolyte applications.<sup>22</sup>

Until recently, much attention has been given to aqueous RFBs, which tended to be mainly limited by slower electrochemical kinetics.<sup>23</sup> As such, the design of electrodes for this class has been largely carried out for facile kinetics over the years and has witnessed significant success.<sup>24–31</sup>

Although less studied in the past, mass transport in RFBs is gaining increased consideration as a performance-limiting factor. Poor mass transport causes overpotentials in RFBs due to insufficient electrolyte accessibility to electrode surfaces. Like surface chemistry in the case of electrochemical kinetics, the electrode's physical microstructure plays an important role in effective mass transport.<sup>32</sup> RFBs' performance in relation to electrode microstructure has been evaluated by several researchers.<sup>33–38</sup> These studies predominantly employing conventional carbon-based electrodes (paper, felt, and cloth) revealed that electrode porosity, pore sizes, and morphologies have significant effects on the transport of reactants, ultimately affecting the electrochemical performance. Comparatively, GAs have hardly been reported for RFBs. Yang et al.<sup>39</sup> showed that macro-meso porous graphene aerogel improved mass transport in the VRFB system. This work relates a focused effort to understand the synthesis of directional graphene aerogel (DGA) electrodes specifically to control pore size and morphology.

1.3. Design and Functioning of GA Electrodes. We see that there has been little emphasis on how to systematically incorporate and control desired characteristics in bottom-up electrode design and synthesis. This is more critical for ORFBs, which preferentially require electrodes with mass transport-optimized features. Note that conventional materials have random pore structures, in contrast to the more ordered structure reported here. Owing to their favorable electrode properties and the ability to be microengineered via simple processing techniques, GAs are believed to be an alternative material for alleviating transport issues in ORFBs.

In RFBs, liquid electrolytes percolate into the microporous spaces of the electrode. Thus, the transport behavior of ions in the electrolyte is influenced by the electrode microstructure. For example, the frequency of the collision of ions with electrode walls increases when they pass through jagged porous regions. At the same time, ion/mass movement may be slowed down after reactants enter narrowed or more jagged pores, and the resulting ion transport times can be longer when the length of the porous pathway increases. All such ion-electrode interactions induce obstacle effects that impede effective ion movement (convective, diffusion, and migration) to and from the electrode reactive sites. With organic reactants, these interactions will be more pronounced due to their larger molecular geometries and higher viscosities. Building on this, we propose "directional" GAs with microstructures specifically tailored to minimize the adverse effects of these interactions on

1.4. Directional Graphene Aerogel (DGA). We envisage that by constructing GAs with directionally aligned porous frameworks, the convective and diffusive flux of organic electroactive species can be significantly improved. We call such a specialized GA a directional graphene aerogel (DGA). In this broader effort, the aim of this work is to understand the physical development and control of directional features in GAs.

Freeze casting of hydrothermally reduced graphene oxide (RGO) is becoming a widely adopted technique for synthesizing GAs owing to its simple steps, high yield, and, notably, the flexibility of synthesis condition, thus allowing for versatile GAs with a wide range of porosity, pore sizes, shapes, and distribution. This approach involves freezing the system of RGO particles in the form of graphene hydrogel (GH) below the freezing temperature of the solvent (usually water). During freezing, the propagating ice fronts reject the particles and concentrate them into the lateral intercrystal spaces. Upon postsolidification removal of the frozen solvent ice, the resulting morphology of GAs is the direct consequence of the growth pattern of ice crystals. Freezing GHs under a one-dimensional (1D) temperature gradient, GAs with a highly oriented pore network or DGAs could be realized.

Freeze casting synthesis parameters have been investigated to achieve GAs with a controlled microstructure. Xie et al. 43 prepared GAs under different freezing temperatures and noted that the mean pore size increased with increasing freezing temperature. Similar observations on pore size dependence on freezing temperatures were reported by Jung et al. 44 Liu et al. 45 investigated the effect of graphene oxide (GO) concentration on the microstructure of GAs. It was confirmed that both the pore size and wall thickness increased with increasing freezing temperature. It was also shown that GAs with thicker walls and larger pores exhibited higher resilience to compressive strain, while those with thinner walls and larger pores had a better adsorption capacity. Liu et al. 46 and Qiu et al. 47 reported that pore size decreased with increased concentration, and the anisotropic structure created with directional freezing showed superior mechanical and electrical properties.

1.5. Scope of the Present Work. Prior studies provide an excellent outlook of freeze casting synthesis conditions on GAs' microstructure. However, what we understand so far is that the graphene—water—ice structuring process is still not very clear and is rarely reported, particularly when the objective is to design and control directional pore channels, i.e., DGAs. Therefore, insights into the microscopic mechanisms that dictate ice crystal growth and directionality during graphene—water freezing will be crucial due to their decisive role in the final porous structure of DGAs.

The aim of this work is to understand the physical development and control of directional features in GAs during the freeze casting process. We investigated freeze casting parameters of the directional freezing temperature, GO loadings, and container aspect ratio to elucidate their effects on the formation and control of porous channels. Directional freezing temperature governs the ice phase change behavior, which relates to the evolution of specific pore attributes. GO loadings represent the active material content of the DGA electrode. Furthermore, the aspect ratio of DGA represents the dimensional limits of the freezing system under which the intended features of DGA could be satisfactorily constructed. These findings will also be useful in optimizing directional porosity in conjunction with system electrochemical characteristics, enabling chemistry-specific DGA electrodes and their functionalization.

#### 2. EXPERIMENTAL SECTION

**2.1. Synthesis of Directional Graphene Aerogel (DGA).** DGA synthesis uses mass-produced graphene oxide (GO) from graphite bulk, typically with Hummers' exfoliation method<sup>48</sup> as precursor material. Research grade aqueous GO was purchased from



Figure 1. Synthesis of DGA via the thermochemical reduction route.

Graphenea, Inc., USA, and had an elemental composition of 52% carbon and 45% oxygen as per the manufacturer. In a typical DGA synthesis procedure (Figure 1), homogeneously dispersed 2 mg/mL GO solution was thoroughly mixed with L-ascorbic acid which acted as a reducing agent (GO/LAA = 1:1) via sonication. <sup>49</sup> The sonicated mixture was transferred to cylindrical glass vials of 12.8 mm internal diameter (2.5 mL volume in each vial) and placed in the oven at 80 °C for 90 min to carry out a thermochemical redox process. Upon completion, the GO mixture was converted to reduced graphene oxide (RGO) with sheets self-assembled in the form of graphene hydrogel (GH) in the vials. The hydrogel was then carefully washed several times with deionized water to remove any LAA residue.

The hydrogel vial was placed on top of the aluminum base, which was immersed in liquid nitrogen. This allowed for unidirectional, progressive freeze casting from the contacting surface upward in the vial. Since the selected vials had near-flat bottoms, additional flattening of the bottom was not attempted. An induction coil heater wrapping the aluminum base was used to control the contact surface temperature, ranging from -20 to -115 °C, to examine the freezing temperature effect. During the freeze-cast, the vial wall was insulated to help the unidirectional vertical temperature gradient with minimum nonuniformity in the lateral temperature distribution. Next, the frozen samples were vacuum freeze-dried for up to 48 h to obtain the final DGA samples. DGA samples with GO loadings ranging from 2 to 10 mg/mL were also synthesized. For example, to synthesize DGA of 4 mg/mL GO, 3 mL of deionized water was added to 2 mL of 10 mg/ mL GO starting suspension. Similarly, to study the aspect ratio effect, samples (2 mg/mL GO) were synthesized in three different with internal diameters of 25, 18.8, and 12.8 mm. The samples were frozen at -20 °C and freeze-dried under the same conditions.

The mean pore sizes of the samples were determined based on the equivalent circle diameter from the pore images taken with a Zeiss Auriga scanning electron microscope using ImageJ software.<sup>50</sup>

# 3. RESULTS AND DISCUSSION

As a basic atomic scale characterization, Raman fingerprinting is discussed to show the carbon structural changes from the precursor GO material to the RGO after DGA synthesis. Successively, the three main synthesis variables and their effects on DGA pore size and directionality are discussed: (1) the freezing temperature, (2) the GO loadings, and (3) the vial aspect ratio.

**3.1. Raman Fingerprinting.** Figure 2 shows Raman fingerprint scanning of both the GO precursor material and the RGO carbon structures of synthesized DGA using a PlanarTECH Raman system with a 532 nm Nd:YAG laser source. Carbonaceous materials display two well-known peaks

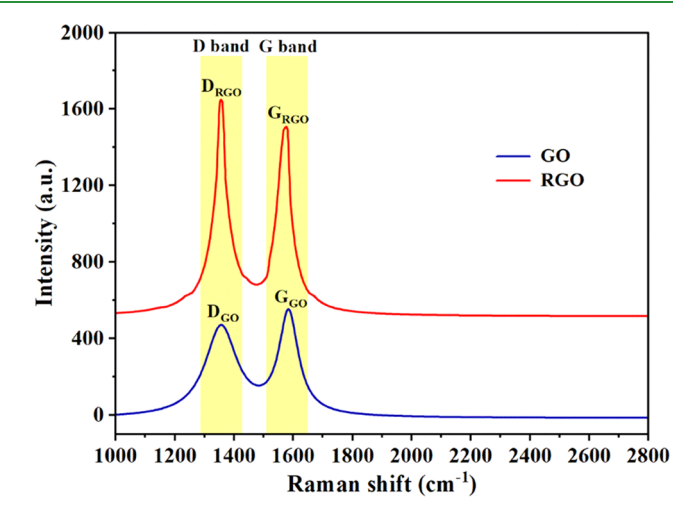


**Figure 2.** Raman spectra of the GO precursor and the RGO of synthesized DGA.

in their Raman spectra: the D peak, related to the disorder, and the G peak, assigned to in-plane vibrations of the sp<sup>2</sup> carbon domains. The D and G peaks for GO appeared at 1356 and 1584 cm<sup>-1</sup>, respectively, with a D/G peak height ratio of 0.88. RGO of DGA also displayed a similar Raman spectrum with D and G peaks at 1342 and 1576 cm<sup>-1</sup>, respectively, but with a D/G peak ratio of 1.16. The D/G peak intensity ratio serves as an indicator of the disorder or recovery within the graphene lattice, reflecting the balance between sp<sup>2</sup> and sp<sup>3</sup> carbon content.<sup>51</sup> Graphene oxide (GO) is structurally more defective (greater sp<sup>3</sup> carbon) due to oxygen-containing groups and therefore conforms with the universal observation that such graphene material exhibits broader D and G bands. While the G mode is present at all sp<sup>2</sup> sites, the intensity of the D mode is directly linked to the existence of 6-fold aromatic rings.<sup>52</sup> Additionally, D/G peak height ratios or integrated area ratios are inversely correlated with the size of sp<sup>2</sup> graphitic regions. 53,54 Consequently, the greater D/G in RGO implied that defects were minimalized during the reduction process, possibly from the removal of oxygen functional groups of GO. This caused the restoration of numerous small yet not fully healed sp<sup>2</sup> rings, 55,56 producing a prominent D peak. Both D and G peaks in RGO became sharper, in comparison with the GO case; this sharpening further indicates that the structure

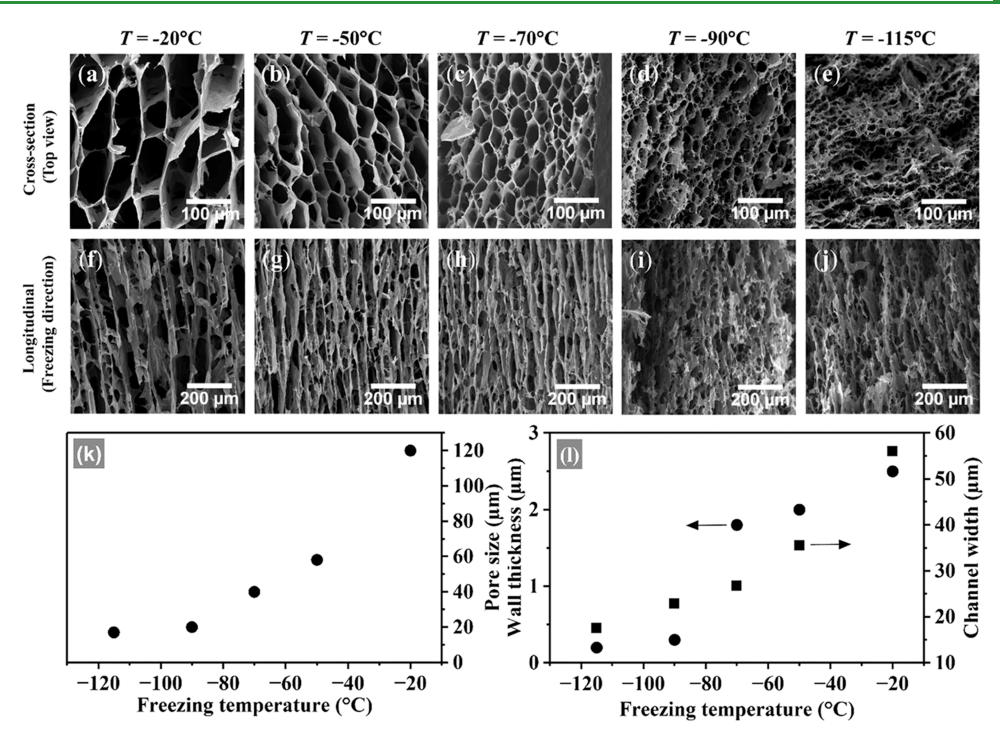


Figure 3. Scanning electron microscopy (SEM) images of DGAs' (2 mg/mL GO) porous network developed at various freezing temperatures. (a– e) Cross section (top view) and (f-j) longitudinal section (freezing direction) pore structures for bottom surface temperatures of -20, -50, -70, -90, and -115 °C, respectively. (k) Mean pore sizes and (l) wall thicknesses and vertical channel widths for each freezing temperature.

amorphousness is reduced (more ordering) with reduced oxygen contents in DGA and shows more graphene-like properties.<sup>57</sup>

Apart from chemical reduction confirmation of GO, D/G peak ratio also relates to the oxygen content in RGO and decreases with consistent removal of oxygen.<sup>58</sup> This removal strongly influences final DGA properties, e.g., DGA electrical conductivity and elasticity improve as oxygen is decreased, since the microstructure is restored with larger graphitic domains, enhancing electron transfer and stacking interactions.<sup>59,60</sup> More atomic scale characterizations including X-ray photoelectron spectroscopy (XPS) and X-ray diffraction (XRD) will be highly beneficial as our future endeavor is realized to examine DGA electrodes for electrochemical performance for ORFB. We, however, currently feel that such atomic scale spectroscopic testing can be somewhat outside the present scope.

Note that certain reduction levels must be achieved to obtain stable GH. In our case, since D/G peak ratio increased and their peak widths decreased, it corresponded to RGO with a lower degree of reduction, that is, "stage 1" reduction<sup>61</sup> but well enough to form stable GH. Here, the elimination of oxygen bonds reduces the defects but is not offset by the reconstruction of larger graphitic layers, which is why there is an increase in the spectral intensity of D band. Increasing the reduction level has an important influence on the structural integrity of GA. For example, high reduction improves compressive and electrical properties<sup>60</sup> but with excessively high reduction, the structural strength goes down with more fragile aerogel as high crystallinity and low defect of graphene sheets cause inadequate interfacial interactions leading to brittleness. 62 Such reductions are commonly achieved by hightemperature thermal annealing.

**3.2. Directional Freezing Temperature.** Porosity, pore sizes, and morphologies are expected to strongly influence the

electrolyte flow distribution with the DGA electrodes. While higher porosity is favorable for electrolyte flow through the electrode, <sup>22</sup> it can diminish the electrode surface area <sup>63,64</sup> and wall thicknesses, <sup>65</sup> impacting electrochemical activity and solid state conduction. To explore control of these DGA pore aspects, we used the parameter of directional freezing temperature, as it strongly influences water—ice structuring kinetics, which are then reflected in the final porous structure.

Figure 3a-e presents microstructures of DGA pores that were formed at different freezing temperatures at the bottom of the vial. It is seen that the pore sizes and morphologies of DGAs are highly dependent on the freezing temperature. When DGAs were frozen at -20 °C (Figure 3a), a mean pore size of 120  $\mu$ m with a lamellar honeycomb-like structure was obtained. When freezing temperatures were decreased to -50and -70 °C, the average pore sizes decreased to 58 and 40  $\mu$ m, respectively, with increasing number of pores and exhibited a mix of semilamellar and elliptical pore morphologies (Figure 3b,c). For further lower freezing temperatures of -90 and -115 °C, the mean pore sizes further decreased to 20 and 17  $\mu$ m, respectively, with similar elliptic morphologies that were somewhat poorly defined (Figure 3d,e). Figure 3k shows the progressive decrease of the mean pore sizes as the freezing temperature decreased from -20 to -115 °C.

The microstructures in the freezing or longitudinal direction are shown in Figure 3f–j. It is clear that the extent of directionality was dependent on the freezing temperature. In the range of -70 to -20 °C, directionality was retained (Figure 3f–h), However, the directionality deteriorated at -90 °C and below (Figure 3h,i). Wall thicknesses and vertical channel widths displayed the same trend as that of pore sizes, both decreasing with decreasing freezing temperatures (Figure 3l). From -20 to -115 °C, DGA wall thickness decreased from 2.5 to 0.2  $\mu$ m while channel widths decreased from 56 to 18  $\mu$ m.

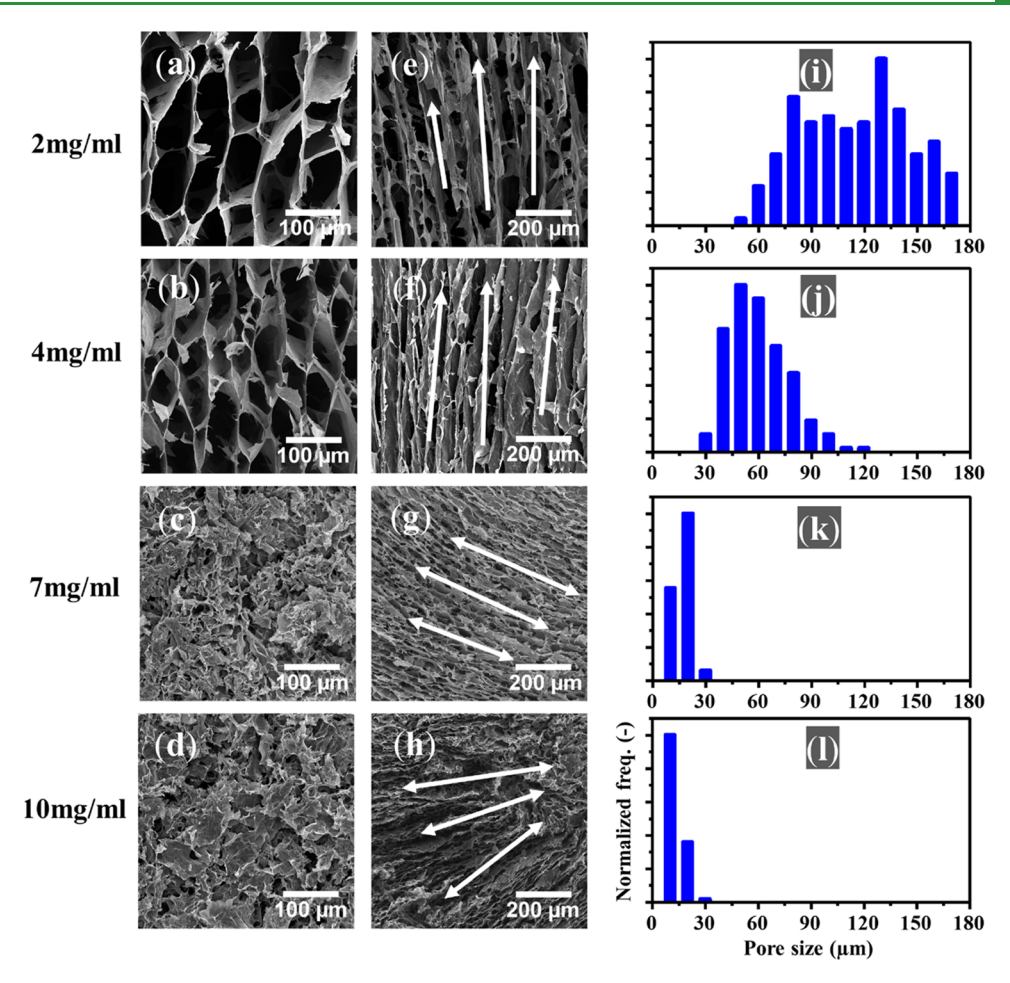


Figure 4. SEM images of DGAs' porous networks for various GO concentrations. The freezing temperature for all of the samples was -20 °C. (a-d) Top view of pore structures, (e-h) longitudinal (freezing direction) view of pore channels, and (i-l) pore size distributions for 2, 4, 7, and 10 mg/mL GO loadings, respectively. White arrows show the paths taken by the ice crystals during freezing.

When graphene hydrogel (GH) is subjected to freezing in a confined vial, ice phase propagation is dependent on a combined effect of nucleation and crystal growth at each temperature. This dependency has been commonly described as lower freezing temperatures causing nucleation to be a dominant influence, restricting growth. The relatively high nucleation rate at a lower temperature causes many smaller ice crystals to produce several small pores. In contrast, when the freezing temperatures increase, steady growth of ice is promoted, leading to larger ice crystals and therefore a smaller number of larger pores.

To enhance our understanding of the multiscale icing mechanisms, ranging from atomic scale nucleation to macroscale crystal/pore growth, we conducted a molecular dynamic (MD) study to predict ice propagation in graphene—water complex fluid. In our recent publication, <sup>66</sup> we demonstrated that the freezing propagation speed can be maximized at an optimum supercooling through MD simulations. As the freezing temperature increases, the mobility of the water molecules increases, while the thermodynamic driving force for the water—ice phase change decreases. The maximum velocity for ice crystal propagation was predicted to be at 252 K (–21 °C) as an optimum combination of these two competing parameters. This MD finding is consistent with the experimental observations (Figure 3) in which the freezing temperature range, from –20 to –50 °C, enabled stable

growth of ice crystals and allowed for larger continuous pores with well-defined lamellar morphology.

On the other hand, at lower freezing temperatures (-70 °C and below), the dominating thermodynamic driving force rapidly generated more crowded ice crystals and impeded the stable growth of individual crystals. This led to smaller pores with thin pore walls. Also, ice crystals under rapid nucleation conditions at lower temperatures were not strong enough and underwent breakdowns.<sup>67</sup> This explains why the pore structure became ill-defined as the freezing temperature decreased.

Freezing temperature will be decisive to the mass transport capabilities of DGAs. For example, under fixed RFB operating conditions, electrolyte flow in DGAs synthesized at low freezing temperatures ( $>-70~^{\circ}\text{C}$ ) will become more compromised as small pores and nonuniformities of transport channels would offer more resistance to flow.

**3.3. Graphene Oxide Loadings.** The amount of active material (RGO) is a major electrode design parameter. GO loadings directly affect the area of electrochemically active sites to support electrochemical reactions, thus influencing the performance of the electrode. We examined the GO loading effects on DGA structuring during freeze casting.

Different GO loadings produced different pore morphologies (Figure 4a-d), directional attributes (Figure 4e-h), and sizes (Figure 4i-l). 2 mg/mL concentration is represented for comparison (Figure 4a), which had a pore diameter peak

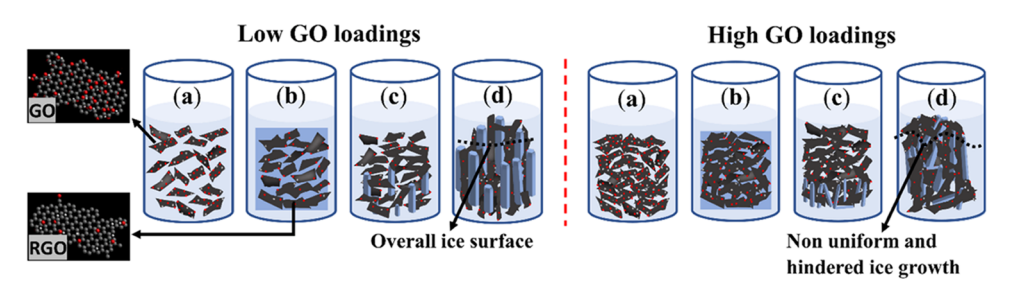


**Figure 5.** Illustration of directional ice propagation in graphene hydrogels (GHs) with low and high GO loadings. (a) GO aqueous solution. (b) RGO sheet assembly in the form of GH. (c) Initial formation of ice crystals during freezing. (d) Growth and directional continuity of ice crystals as the freezing progresses.

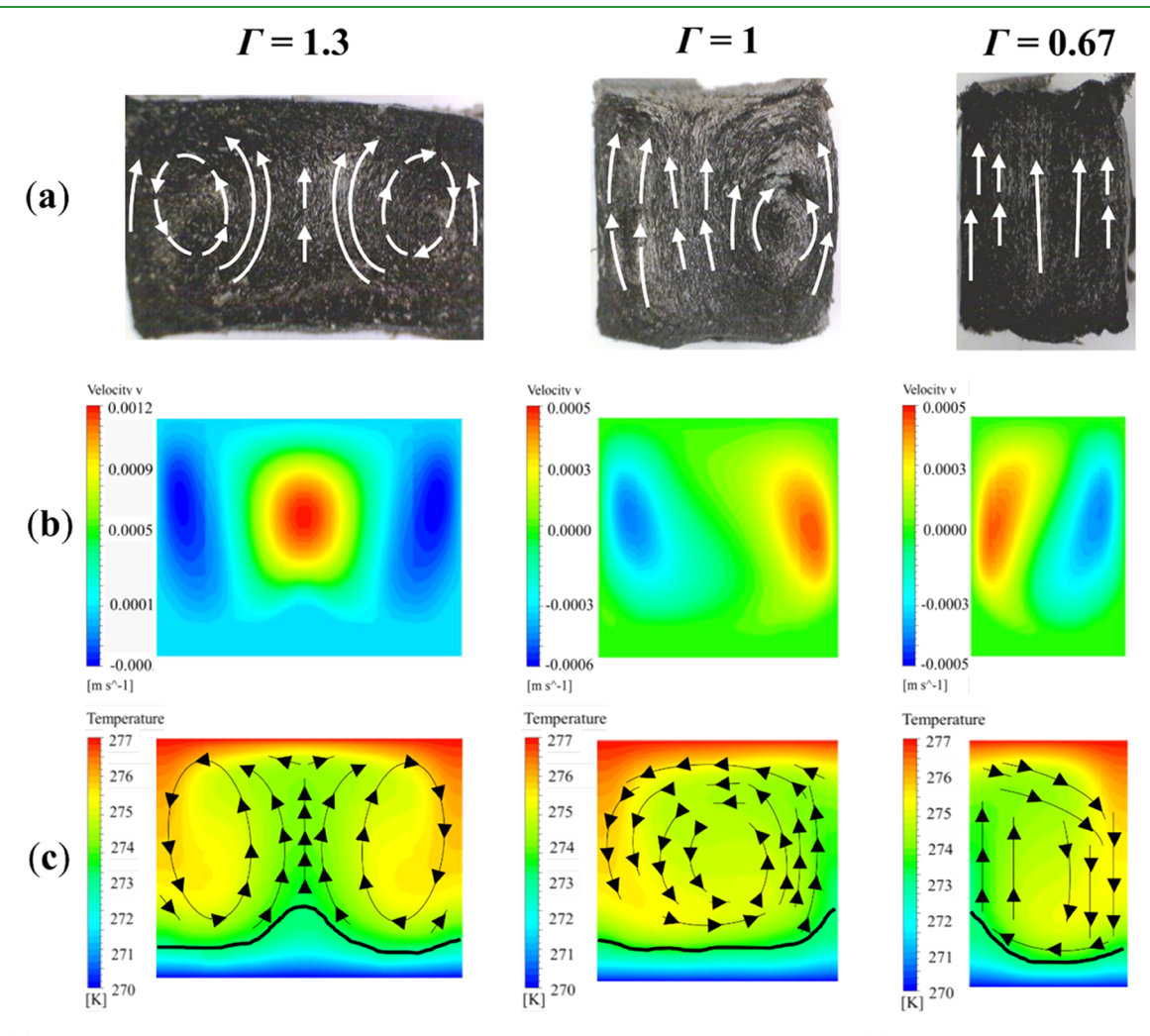


Figure 6. (a) Observed departure of ice crystals from the imposed direction of growth under various  $\Gamma$ . (b) Corresponding velocity profiles caused by temperature distributions (c) for each  $\Gamma$  at the end of simulation time (1200 s). Velocity profiles display the convection flow. The structure of the water—ice interface is also shown (marked with solid black curves). Black arrow lines represent streamlines in accordance with the respective velocity profiles. The simulated water container height was fixed at 18.8 mm, and the vial diameter was varied from 25 to 12.8 mm. Container bottom and top temperatures were 270 and 277 K, respectively. The walls of the container were assumed to be adiabatic.

between 80 and 130  $\mu$ m (Figure 4i). The dominant pore peak for 4 mg/mL loading (Figure 4b) was between 40 and 60  $\mu$ m with certain size variations (Figure 4j). For 7 and 10 mg/mL loadings (Figure 4c,d), the pore sizes decreased to a range of 10–20  $\mu$ m with relatively fewer variations (Figure 4k,l).

Morphological changes were also noted. For DGAs with 2 and 4 mg/mL GO loadings, pore interconnectedness was stretched over longer vertical length scales (Figure 4e,f) than DGAs synthesized with 7 mg/mL loadings and above (Figure

4g,h). This means that long-range directional interconnectivity between pores was feasible up to certain concentration limits, but beyond them, the ice could not sustain vertical growth. These results suggest that the unidirectional propagation of ice was limited by increasing GO loading.

The experimental observation of GO loading effects on the directionality of DGAs can be explained with the illustration in Figure 5. For low GO loadings, the greater interflake spacing with greater water content facilitates the transport of water

molecules via self-diffusion to join the ice front. The fluxes directionally normal to prism as well as basal planes extend the growth of individual ice crystals over a larger distance  $(y_m)$ . This directional growth is due to solidification fronts rejecting loosely packed particles, allowing for larger pore dimensions with long-range interconnectedness for low GO loadings.

When loadings are high, ice growth is suppressed due to the high resistance of densely packed RGO particles and the low water content between these particles. Additionally, in a closed packing environment, the phase change temperature of the water—ice interfaces depresses. These factors inhibit the ice crystals from gaining the sufficient propagation velocities required to penetrate particle clusters. As such, the growth of ice crystals will not be directionally uniform, as they either locally nucleate with small interparticle spacings or scatter in multiple directions, producing small pores and discontinuous network channels. The increased variations of the ice surface further support the notion that ice cannot sustain long-range directionality at high GO loadings.

Optimal GO loadings will be necessary for directional control of transport pathways in DGAs and for retaining other performance properties such as overall porosity and surface area. In general, while low GO content promotes pore directionality, excessively low GO contents must be avoided to support the electrode's core needs: high surface area, porosity, and mechanical/electrochemical stability. Our investigation suggests that a GO loading of approximately 4 mg/mL is a good optimum in preserving GA pore directionality as well as an acceptable mass density. However, future evaluation of DGA-4 mg/mL electrode is a must along with other loadings in the ORFB setup to validate our optimal concentration claim.

**3.4. Aspect Ratio.** In addition to graphene oxide loading, the aspect ratio of the freezing vessel/domain was explored. The dimension of the freezing domain corresponds to the final size of a freeze-cast structure; i.e., larger samples are synthesized in larger freezing domains. Nevertheless, as freezing vessel dimensions increase, the temperature field becomes more vulnerable to instabilities, influencing freezing kinetics. During freezing, convection currents can form, and these currents influence the resulting microstructure of a freeze-cast DGA. The geometric dimensions of the freezing vessel can influence the velocities of these convection currents, providing a means of controlling DGA structure. As such, a parameter of the container aspect ratio was used to clarify the role of freezing dimensions on ice structuring.

Figure 6a shows synthesized DGA samples with three different vial diameter-to-height aspect ratios ( $\Gamma=D/H$ ) for a constant 2 mg/mL GO loading. For the tested  $\Gamma=1.33$ , 1.0, and 0.68, the vial height H remained the same at 18.8 mm while the vial diameter D was decreased. Larger  $\Gamma$  showed more curvaceous or tortuous pores compared to smaller  $\Gamma$ . The stronger convection rolls with a larger  $\Gamma$  interrupted the directional growth of ice crystals in the vertical direction. In contrast, a smaller  $\Gamma$  constrained the convection rolls, enabling more uniformly directional pore growth.

Water freezing simulations were conducted to examine the effect of  $\Gamma$  on the convection roll formations and their strengths using the built-in solver in Ansys-Fluent (ANSYS, Inc.). The finite volume method (FVM) was employed to solve the mass, momentum, and energy conservation equations. The properties of water (density, viscosity, and thermal conductivity) were considered temperature-depend-

ent. To For all three aspect ratios, the bottom and top surfaces were maintained at 270 and 277 K, respectively, and the side walls were assumed to be adiabatic. The flow behavior during freezing for each  $\Gamma$  was examined. Figure 6b,6c presents the calculated velocity contour maps and temperature distribution at 1200 s after the freezing began; the ice—water interface is represented by the solid curve in each of the temperature contour maps.

The corresponding Rayleigh number  $(Ra = |\rho g\beta H^3 \Delta T|/\alpha \mu)$ of  $1.1 \times 10^5$  exceeded the critical range for the onset of the convective rolls ( $Ra_{cr} = 10^3 - 10^4$ ), <sup>71,72</sup> where  $\rho$  is the density of water (999.855 kg/m $^3$ ), g is the gravitational acceleration (9.81 m/s<sup>2</sup>),  $\beta$  is the thermal expansion coefficient (-5.598 × 10<sup>-5</sup>/ K),  $\Delta T$  is the temperature difference from the bottom and top surfaces (-7 K), H is the height of the filled solution (0.02 m),  $\alpha$  is the thermal diffusivity (1.32 × 10<sup>-7</sup> m<sup>2</sup>/s), and  $\mu$  is the dynamic viscosity (1.32  $\times$  10<sup>-7</sup> kg/m·s). The combination of cold temperature at the bottom and elevated temperature at the top surface contributed to the distinct density-temperature relationship of water (maximum density at 4 °C), triggering the Rayleigh-Bénard convection. The computed convection patterns strikingly resembled the measured pore patterns and their directions. For  $\Gamma$  = 1.3, two strong symmetric convection rolls developed with a maximum flow speed of up to 1.2 cm/s. These strong convection rolls interrupted and restricted directional icing propagation, as shown by the pore structure in Figure 6a. When  $\Gamma$  was reduced to 1.0, a single convection roll developed with a reduced maximum flow speed of about 0.4 cm/s yet still interrupted the directional growth of the pores. When  $\Gamma$  was further lowered to 0.68, the convection roll became confined, primarily due to the precedence of the viscous drag in a narrowed-in area with (D) and the resulting flow patterns were nearly parallel to form highly directional pore structures, except for the very top and bottom regions where lateral flows were inevitable.

The aspect ratio analysis revealed that graphene flakes align with the convective flow streamlines due to the forces exerted by the flow on the flakes. Rayleigh—Bénard convection, stemming from the unique density—temperature relationship of water, manifests in the freezing process characterized by a cold bottom temperature, thereby impacting the alignment of graphene flakes prior to freezing. As the Rayleigh—Bénard convection flow pattern is known to depend on the aspect ratio, and not necessarily on the individual combinations of width and height dimensions, we anticipate similar convection behavior with the same aspect ratio, even when the height or diameter varies individually. However, exploring more diverse cases, encompassing concurrent changes in height, diameter, and temperature, can enhance the comprehensiveness of this research.

It is known that effective ion diffusivity is inversely proportional to the tortuosity of pores, increasing the effective transport path length. Increased pore tortuosity makes the ions replenish the rapidly depleted reactive sites more slowly. As noted previously, electrode surface area increases for thicker/denser electrodes; however, mass transport limits the maximum electrode thickness and/or density. Therefore, the use of a slender vial with a low  $\Gamma$  will be advantageous in fabricating DGAs with low pore tortuosity, enhancing mass transport throughout the porous electrode structure.

#### 4. CONCLUSIONS

In this work, freeze casting has been employed to synthesize and characterize GAs with directionally oriented porous microstructures. The overarching aim was to understand the structural development and control of directional features in directional graphene aerogels (DGAs) with freeze casting. It is revealed that the stability and morphology of solidifying water—ice interfaces are affected by freezing temperature, water—ice—graphene interactions, and interfacial convective heat transfer.

Pore sizes, pore morphologies, pore wall thicknesses, and the directionality of pores can be largely regulated by the freezing temperatures and ascribed to the ice growth dynamics controlled by the competition between the self-diffusivity of water and the phase change driving forces at a given temperature. By controlling temperature, the relative prevalence of these competing phenomena can be tweaked for the nucleation and growth rate, which encourages directional ice propagation and so the pores. For the freezing temperature range from -20 to  $-115\,^{\circ}\text{C}$ , 6-fold decrease in pore sizes was observed with decreasing temperature. For freezing temperatures below  $-70\,^{\circ}\text{C}$ , the pore directionality was poor due to irregular growth of ice crystals.

With increasing GO loading, the dense particle packing interferes with ice growth, resulting in the loss of overall porosity and pore alignment. While lower GO loadings promote macroporosity, which can enhance mass transport when used for ORFBs, they may compromise DGAs' structural integrity as well as electrochemical activity due to reduced surface areas. Achieving a balance of these DGA performance attributes requires maximum GO concentration, which not only improves mass density but also supports directional propagation of ice and was proposed to be 4 mg/mL. However, actual tests are inevitable to confirm this optimality.

This work also demonstrated the major influence of the synthesis vessel aspect ratio on DGA pore morphology. Increased vial diameter-to-height ratio ( $\Gamma$ ) caused flow in the liquid region above the water—ice interface which interrupted ice crystals from the desired direction of growth. Hence, more tortuous pore channels formed when  $\Gamma$  increased. The use of  $\Gamma$  less than unity could alleviate the adverse effects of convection on ice propagation.

In conclusion, this study explored the effective control of ice growth mechanisms for the fabrication of DGAs with desirable pore sizes and morphologies, maximum active material utilization, and directional pore connectivity. The results show significant potential for the directional design of materials where enhanced mass transport capabilities are required, such as electrodes for organic redox flow batteries and membranes where controlled pore size and distribution are critical for efficient separation processes. Solvent-dependent ice propagation kinetics would be interesting to consider for effective DGAs; therefore, in the future, we recommend the synthesis of DGAs in various nonaqueous solvents of low freezing temperatures for investigating directionality.

# AUTHOR INFORMATION

### **Corresponding Authors**

Mian U. Saeed – Department of Mechanical, Aerospace and Biomedical Engineering, University of Tennessee, Knoxville 37996 Tennessee, United States; orcid.org/0009-0002-2554-2263; Email: msaeed2@vols.utk.edu

Kenneth D. Kihm — Department of Mechanical, Aerospace and Biomedical Engineering, University of Tennessee, Knoxville 37996 Tennessee, United States; orcid.org/ 0000-0001-5360-1764; Email: kkihm@utk.edu

#### **Authors**

- Yu-Kai Weng Department of Mechanical, Aerospace and Biomedical Engineering, University of Tennessee, Knoxville 37996 Tennessee, United States
- Mohammad Bahzad Department of Mechanical, Aerospace and Biomedical Engineering, University of Tennessee, Knoxville 37996 Tennessee, United States
- Seungha Shin Department of Mechanical, Aerospace and Biomedical Engineering, University of Tennessee, Knoxville 37996 Tennessee, United States; orcid.org/0000-0002-0971-9797
- Doug S. Aaron Department of Mechanical, Aerospace and Biomedical Engineering, University of Tennessee, Knoxville 37996 Tennessee, United States

Complete contact information is available at: https://pubs.acs.org/10.1021/acsami.3c10998

#### **Author Contributions**

M.U.S.: Experimental investigations, formal analysis, writing—original draft. Y.-K.W.: Software, validation, formal analysis, writing—review and editing. M.B. Experimental investigations, writing—review and editing. S.S.: Funding acquisition, software, writing—review and editing. D.S.A.: Funding acquisition, conceptualization, supervision, writing—review and editing. K.D.K.: Funding acquisition, conceptualization, supervision, project administration, writing—review and editing.

#### Notes

The authors declare no competing financial interest.

# ■ ACKNOWLEDGMENTS

The authors gratefully acknowledge the financial support by the U.S. National Science Foundation for this research (grant no. CBET-1933800).

## **■** REFERENCES

- (1) Ai, S.; Chen, Y.; Liu, Y.; Zhang, Q.; Xiong, L.; Huang, H.; Li, L.; Yu, X.; Wei, L. Facile Synthesis of Nitrogen-Doped Graphene Aerogels for Electrochemical Detection of Dopamine. *Solid State Sci.* **2018**, *86*, 6–11.
- (2) Singh, E.; Nalwa, H. S. Graphene-Based Dye-Sensitized Solar Cells: A Review. Sci. Adv. Mater. 2015, 7 (10), 1863–1912.
- (3) Fu, X.; Choi, J.-Y.; Zamani, P.; Jiang, G.; Hoque, M. A.; Hassan, F. M.; Chen, Z. Co-N Decorated Hierarchically Porous Graphene Aerogel for Efficient Oxygen Reduction Reaction in Acid. ACS Appl. Mater. Interfaces 2016, 8 (10), 6488-6495.
- (4) Lu, Y.; Yang, Y.; Zhang, T.; Ge, Z.; Chang, H.; Xiao, P.; Xie, Y.; Hua, L.; Li, Q.; Li, H.; et al. Photoprompted Hot Electrons from Bulk Cross-Linked Graphene Materials and Their Efficient Catalysis for Atmospheric Ammonia Synthesis. *ACS Nano* **2016**, *10* (11), 10507–10515.
- (5) Im, H.; Kim, T.; Song, H.; Choi, J.; Park, J. S.; Ovalle-Robles, R.; Yang, H. D.; Kihm, K. D.; Baughman, R. H.; Lee, H. H.; et al. High-Efficiency Electrochemical Thermal Energy Harvester Using Carbon Nanotube Aerogel Sheet Electrodes. *Nat. Commun.* **2016**, *7* (1), No. 10600.
- (6) Yu, C.; Kim, H.; Youn, J. R.; Song, Y. S. Enhancement of Structural Stability of Graphene Aerogel for Thermal Energy Harvesting. ACS Appl. Energy Mater. 2021, 4 (10), 11666–11674.

- (7) Zhan, W.; Yu, S.; Gao, L.; Wang, F.; Fu, X.; Sui, G.; Yang, X. Bioinspired Assembly of Carbon Nanotube into Graphene Aerogel with "Cabbagelike" Hierarchical Porous Structure for Highly Efficient Organic Pollutants Cleanup. ACS Appl. Mater. Interfaces 2018, 10 (1), 1093–1103.
- (8) Luo, Y.; Jiang, S.; Xiao, Q.; Chen, C.; Li, B. Highly Reusable and Superhydrophobic Spongy Graphene Aerogels for Efficient Oil/Water Separation. *Sci. Rep.* **2017**, *7* (1), No. 7162.
- (9) Sui, Z.-Y.; Meng, Y.-N.; Xiao, P.-W.; Zhao, Z.-Q.; Wei, Z.-X.; Han, B.-H. Nitrogen-Doped Graphene Aerogels as Efficient Supercapacitor Electrodes and Gas Adsorbents. ACS Appl. Mater. Interfaces 2015, 7 (3), 1431–1438.
- (10) Bard, A. J.; Faulkner, L. R.; White, H. S. Electrochemical Methods: Fundamentals and Applications; John Wiley & Sons, 2022.
- (11) Wei, X.; Duan, W.; Huang, J.; Zhang, L.; Li, B.; Reed, D.; Xu, W.; Sprenkle, V.; Wang, W. A High-Current, Stable Nonaqueous Organic Redox Flow Battery. ACS Energy Lett. 2016, 1 (4), 705–711.
- (12) Winsberg, J.; Hagemann, T.; Janoschka, T.; Hager, M. D.; Schubert, U. S. Redox-Flow Batteries: From Metals to Organic Redox-Active Materials. *Angew. Chem., Int. Ed.* **2017**, *56* (3), 686–711
- (13) Rychcik, M.; Skyllas-Kazacos, M. Characteristics of a New All-Vanadium Redox Flow Battery. *J. Power Sources* **1988**, 22 (1), 59–67.
- (14) Ulaganathan, M.; Aravindan, V.; Yan, Q.; Madhavi, S.; Skyllas-Kazacos, M.; Lim, T. M. Recent Advancements in All-Vanadium Redox Flow Batteries. *Adv. Mater. Interfaces* **2016**, 3 (1), No. 1500309.
- (15) Wu, M.; Zhao, T.; Jiang, H.; Zeng, Y.; Ren, Y. High-Performance Zinc Bromine Flow Battery Via Improved Design of Electrolyte and Electrode. *J. Power Sources* **2017**, *355*, 62–68.
- (16) Chen, H.; Cong, G.; Lu, Y.-C. Recent Progress in Organic Redox Flow Batteries: Active Materials, Electrolytes and Membranes. *J. Energy Chem.* **2018**, 27 (5), 1304–1325.
- (17) Wei, X.; Xu, W.; Vijayakumar, M.; Cosimbescu, L.; Liu, T.; Sprenkle, V.; Wang, W. Tempo-Based Catholyte for High-Energy Density Nonaqueous Redox Flow Batteries. *Adv. Mater.* **2014**, *26* (45), 7649–7653.
- (18) Hu, B.; DeBruler, C.; Rhodes, Z.; Liu, T. L. Long-Cycling Aqueous Organic Redox Flow Battery (Aorfb) toward Sustainable and Safe Energy Storage. *J. Am. Chem. Soc.* **2017**, *139* (3), 1207–1214.
- (19) Wei, X.; Xu, W.; Huang, J.; Zhang, L.; Walter, E.; Lawrence, C.; Vijayakumar, M.; Henderson, W. A.; Liu, T.; Cosimbescu, L.; et al. Radical Compatibility with Nonaqueous Electrolytes and Its Impact on an All-Organic Redox Flow Battery. *Angew. Chem., Int. Ed.* **2015**, 54 (30), 8684–8687.
- (20) Milshtein, J. D.; Tenny, K. M.; Barton, J. L.; Drake, J.; Darling, R. M.; Brushett, F. R. Quantifying Mass Transfer Rates in Redox Flow Batteries. *J. Electrochem. Soc.* **2017**, *164* (11), No. E3265.
- (21) Milshtein, J. D.; Barton, J. L.; Carney, T. J.; Kowalski, J. A.; Darling, R. M.; Brushett, F. R. Towards Low Resistance Nonaqueous Redox Flow Batteries. *J. Electrochem. Soc.* **2017**, *164* (12), A2487.
- (22) Zhou, X.; Zhao, T.; An, L.; Zeng, Y.; Wei, L. Critical Transport Issues for Improving the Performance of Aqueous Redox Flow Batteries. *J. Power Sources* **2017**, 339, 1–12.
- (23) Sum, E.; Skyllas-Kazacos, M. A Study of the V (Ii)/V (Iii) Redox Couple for Redox Flow Cell Applications. *J. Power Sources* **1985**, *15* (2–3), 179–190.
- (24) Sun, B.; Skyllas-Kazacos, M. Modification of Graphite Electrode Materials for Vanadium Redox Flow Battery Application-I. Thermal Treatment. *Electrochim. Acta* **1992**, *37* (7), 1253–1260.
- (25) Pezeshki, A. M.; Clement, J. T.; Veith, G. M.; Zawodzinski, T. A.; Mench, M. M. High Performance Electrodes in Vanadium Redox Flow Batteries through Oxygen-Enriched Thermal Activation. *J. Power Sources* **2015**, *294*, 333–338.
- (26) Sun, B.; Skyllas-Kazacos, M. Chemical Modification of Graphite Electrode Materials for Vanadium Redox Flow Battery Application—Part Ii. Acid Treatments. *Electrochim. Acta* **1992**, *37* (13), 2459—2465.

- (27) He, Z.; Jiang, Y.; Li, Y.; Zhu, J.; Zhou, H.; Meng, W.; Wang, L.; Dai, L. Carbon Layer-Exfoliated, Wettability-Enhanced, So3h-Functionalized Carbon Paper: A Superior Positive Electrode for Vanadium Redox Flow Battery. *Carbon* **2018**, *127*, 297–304.
- (28) Kim, K. J.; Kim, Y.-J.; Kim, J.-H.; Park, M.-S. The Effects of Surface Modification on Carbon Felt Electrodes for Use in Vanadium Redox Flow Batteries. *Mater. Chem. Phys.* **2011**, *131* (1–2), 547–553.
- (29) Dixon, D.; Babu, D.; Langner, J.; Bruns, M.; Pfaffmann, L.; Bhaskar, A.; Schneider, J.; Scheiba, F.; Ehrenberg, H. Effect of Oxygen Plasma Treatment on the Electrochemical Performance of the Rayon and Polyacrylonitrile Based Carbon Felt for the Vanadium Redox Flow Battery Application. *J. Power Sources* **2016**, 332, 240–248.
- (30) Aaron, D.; Yeom, S.; Kihm, K. D.; Gandomi, Y. A.; Ertugrul, T.; Mench, M. M. Kinetic Enhancement Via Passive Deposition of Carbon-Based Nanomaterials in Vanadium Redox Flow Batteries. *J. Power Sources* **2017**, *366*, 241–248.
- (31) Daugherty, M. C.; Gu, S.; Aaron, D. S.; Mallick, B. C.; Gandomi, Y. A.; Hsieh, C.-T. Decorating Sulfur and Nitrogen Co-Doped Graphene Quantum Dots on Graphite Felt as High-Performance Electrodes for Vanadium Redox Flow Batteries. *J. Power Sources* **2020**, 477, No. 228709.
- (32) Forner-Cuenca, A.; Brushett, F. R. Engineering Porous Electrodes for Next-Generation Redox Flow Batteries: Recent Progress and Opportunities. *Curr. Opin. Electrochem.* **2019**, *18*, 113–122.
- (33) Kok, M. D. R.; Khalifa, A.; Gostick, J. T. Multiphysics Simulation of the Flow Battery Cathode: Cell Architecture and Electrode Optimization. *J. Electrochem. Soc.* **2016**, *163* (7), A1408.
- (34) Zhou, X.; Zhao, T.; Zeng, Y.; An, L.; Wei, L. A Highly Permeable and Enhanced Surface Area Carbon-Cloth Electrode for Vanadium Redox Flow Batteries. *J. Power Sources* **2016**, 329, 247—254.
- (35) Zhou, X.; Zeng, Y.; Zhu, X.; Wei, L.; Zhao, T. A High-Performance Dual-Scale Porous Electrode for Vanadium Redox Flow Batteries. *J. Power Sources* **2016**, *325*, 329–336.
- (36) Forner-Cuenca, A.; Penn, E. E.; Oliveira, A. M.; Brushett, F. R. Exploring the Role of Electrode Microstructure on the Performance of Non-Aqueous Redox Flow Batteries. *J. Electrochem. Soc.* **2019**, *166* (10), A2230.
- (37) Zhang, D.; Forner-Cuenca, A.; Taiwo, O. O.; Yufit, V.; Brushett, F. R.; Brandon, N. P.; Gu, S.; Cai, Q. Understanding the Role of the Porous Electrode Microstructure in Redox Flow Battery Performance Using an Experimentally Validated 3d Pore-Scale Lattice Boltzmann Model. *J. Power Sources* **2020**, 447, No. 227249.
- (38) Qiu, G.; Dennison, C.; Knehr, K.; Kumbur, E.; Sun, Y. Pore-Scale Analysis of Effects of Electrode Morphology and Electrolyte Flow Conditions on Performance of Vanadium Redox Flow Batteries. *J. Power Sources* **2012**, *219*, 223–234.
- (39) Yang, Y.; Ma, W.; Zhang, T.; Ye, D.; Chen, R.; Zhu, X. Pore Engineering of Graphene Aerogels for Vanadium Redox Flow Batteries. *Chem. Commun.* **2020**, *56* (95), 14984–14987.
- (40) Shao, G.; Hanaor, D. A.; Shen, X.; Gurlo, A. Freeze Casting: From Low-Dimensional Building Blocks to Aligned Porous Structures—a Review of Novel Materials, Methods, and Applications. *Adv. Mater.* **2020**, 32 (17), No. 1907176.
- (41) Li, W. L.; Lu, K.; Walz, J. Freeze Casting of Porous Materials: Review of Critical Factors in Microstructure Evolution. *Int. Mater. Rev.* **2012**, *57* (1), 37–60.
- (42) Ma, Y.; Chen, Y. Three-Dimensional Graphene Networks: Synthesis, Properties and Applications. *Natl. Sci. Rev.* **2015**, 2 (1), 40–53.
- (43) Xie, X.; Zhou, Y.; Bi, H.; Yin, K.; Wan, S.; Sun, L. Large-Range Control of the Microstructures and Properties of Three-Dimensional Porous Graphene. *Sci. Rep.* **2013**, *3* (1), No. 2117.
- (44) Jung, S. M.; Mafra, D. L.; Lin, C.-T.; Jung, H. Y.; Kong, J. Controlled Porous Structures of Graphene Aerogels and Their Effect on Supercapacitor Performance. *Nanoscale* **2015**, 7 (10), 4386–4393.
- (45) Liu, X.; Pang, K.; Yang, H.; Guo, X. Intrinsically Microstructured Graphene Aerogel Exhibiting Excellent Mechanical

- Performance and Super-High Adsorption Capacity. Carbon 2020, 161, 146–152.
- (46) Liu, T.; Huang, M.; Li, X.; Wang, C.; Gui, C.-X.; Yu, Z.-Z. Highly Compressible Anisotropic Graphene Aerogels Fabricated by Directional Freezing for Efficient Absorption of Organic Liquids. *Carbon* **2016**, *100*, 456–464.
- (47) Qiu, L.; Liu, J. Z.; Chang, S. L.; Wu, Y.; Li, D. Biomimetic Superelastic Graphene-Based Cellular Monoliths. *Nat. Commun.* **2012**, 3 (1), No. 1241.
- (48) Hummers, W. S., Jr; Offeman, R. E. Preparation of Graphitic Oxide. J. Am. Chem. Soc. 1958, 80 (6), 1339.
- (49) Zhang, J.; Yang, H.; Shen, G.; Cheng, P.; Zhang, J.; Guo, S. Reduction of Graphene Oxide Via L-Ascorbic Acid. *Chem. Commun.* **2010**, *46* (7), 1112–1114.
- (50) Schneider, C. A.; Rasband, W. S.; Eliceiri, K. W. NIH Image to Imagej: 25 Years of Image Analysis. *Nat. Methods* **2012**, 9 (7), 671–675.
- (51) Kudin, K. N.; Ozbas, B.; Schniepp, H. C.; Prud'Homme, R. K.; Aksay, I. A.; Car, R. Raman Spectra of Graphite Oxide and Functionalized Graphene Sheets. *Nano Lett.* **2008**, 8 (1), 36–41.
- (52) Ferrari, A. C.; Robertson, J. Interpretation of Raman Spectra of Disordered and Amorphous Carbon. *Phys. Rev. B* **2000**, *61* (20), 14095.
- (53) Tuinstra, F.; Koenig, J. L. Raman Spectrum of Graphite. *J. Chem. Phys.* **1970**, 53 (3), 1126–1130.
- (54) Shen, A.-L.; Weng, Y.-C.; Chou, T.-C. Effect of the Analytic Regions on the Quality Trend of Diamond-Like/Graphitic Carbon Ratios in Raman Spectra. Z. Naturforsch., B 2010, 65 (1), 67–71.
- (55) Ferrari, A. C.; Basko, D. M. Raman Spectroscopy as a Versatile Tool for Studying the Properties of Graphene. *Nat. Nanotechnol.* **2013**, 8 (4), 235–246.
- (56) Krishnamoorthy, K.; Veerapandian, M.; Yun, K.; Kim, S.-J. The Chemical and Structural Analysis of Graphene Oxide with Different Degrees of Oxidation. *Carbon* **2013**, *53*, 38–49.
- (57) Merlen, A.; Buijnsters, J. G.; Pardanaud, C. A Guide to and Review of the Use of Multiwavelength Raman Spectroscopy for Characterizing Defective Aromatic Carbon Solids: From Graphene to Amorphous Carbons. *Coatings* **2017**, *7* (10), 153.
- (58) López-Díaz, D.; Lopez Holgado, M.; García-Fierro, J. L.; Velázquez, M. M. Evolution of the Raman Spectrum with the Chemical Composition of Graphene Oxide. *J. Phys. Chem. C* **2017**, 121 (37), 20489–20497.
- (59) Liu, W.; Speranza, G. Tuning the Oxygen Content of Reduced Graphene Oxide and Effects on Its Properties. ACS Omega 2021, 6 (9), 6195–6205.
- (60) Li, C.; Ding, M.; Zhang, B.; Qiao, X.; Liu, C.-Y. Graphene Aerogels That Withstand Extreme Compressive Stress and Strain. *Nanoscale* **2018**, *10* (38), 18291–18299.
- (61) Díez-Betriu, X.; Álvarez-García, S.; Botas, C.; Álvarez, P.; Sánchez-Marcos, J.; Prieto, C.; Menéndez, R.; De Andrés, A. Raman Spectroscopy for the Study of Reduction Mechanisms and Optimization of Conductivity in Graphene Oxide Thin Films. *J. Mater. Chem. C* **2013**, *1* (41), 6905–6912.
- (62) Peng, L.; Xu, Z.; Liu, Z.; Guo, Y.; Li, P.; Gao, C. Ultrahigh Thermal Conductive yet Superflexible Graphene Films. *Adv. Mater.* **2017**, 29 (27), No. 1700589.
- (63) Weber, A. Z.; Mench, M. M.; Meyers, J. P.; Ross, P. N.; Gostick, J. T.; Liu, Q. Redox Flow Batteries: A Review. J. Appl. Electrochem. 2011, 41 (10), 1137–1164.
- (64) Bu, F.; Shakir, I.; Xu, Y. 3D Graphene Composites for Efficient Electrochemical Energy Storage. *Adv. Mater. Interfaces* **2018**, 5 (15), No. 1800468.
- (65) Jo, C.; Park, Y.; Jeong, J.; Lee, K. T.; Lee, J. Structural Effect on Electrochemical Performance of Ordered Porous Carbon Electrodes for Na-Ion Batteries. *ACS Appl. Mater. Interfaces* **2015**, 7 (22), 11748–11754.
- (66) Weng, Y.-K.; Shin, S.; Kihm, K. D.; Bahzad, M.; Aaron, D. S. Investigation of Microscopic Mechanisms for Water-Ice Phase

- Change Propagation Control. Int. J. Heat Mass Transfer 2022, 184, No. 122357.
- (67) Deville, S.; Adrien, J.; Maire, E.; Scheel, M.; Di Michiel, M. Time-Lapse, Three-Dimensional in Situ Imaging of Ice Crystal Growth in a Colloidal Silica Suspension. *Acta Mater.* **2013**, *61* (6), 2077–2086.
- (68) Peppin, S. S. L.; Elliott, J.; Worster, M. G. Solidification of Colloidal Suspensions. *J. Fluid Mech.* **2006**, *554*, 147–166.
- (69) Deville, S.; Saiz, E.; Tomsia, A. P. Ice-Templated Porous Alumina Structures. *Acta Mater.* **2007**, *55* (6), 1965–1974.
- (70) Weast, R. C.; Astle, M. J.; Beyer, W. CRC Handbook of Chemistry and Physics; Beyer, W. H., Eds.; Chemical Rubber Company Press: Boca Baton, FL, 1982; Vol. 12, p 192.
- (71) Trevisan, O. V.; Bejan, A. Mass and Heat Transfer by High Rayleigh Number Convection in a Porous Medium Heated from Below. *Int. J. Heat Mass Transfer* **1987**, *30* (11), 2341–2356.
- (72) Shishkina, O. Rayleigh-Bénard Convection: The Container Shape Matters. *Phys. Rev. Fluids* **2021**, 6 (9), No. 090502.
- (73) Mutabazi, İ.; Wesfreid, J. E.; Guyon, E. Dynamics of Spatio-Temporal Cellular Structures: Henri Bénard Centenary Review; Springer, 2010.
- (74) Saito, Y. Ion Transport in Solid Medium-Evaluation of Ionic Mobility for Design of Ion Transport Pathways in Separator and Gel Electrolyte. *Membranes* **2021**, *11* (4), 277.
- (75) Yoon, S. J.; Kim, S.; Kim, D. K. Optimization of Local Porosity in the Electrode as an Advanced Channel for All-Vanadium Redox Flow Battery. *Energy* **2019**, *172*, 26–35.

# ☐ Recommended by ACS

Transmission Mechanism and Logical Operation of Graphene-Doped Poly(vinyl alcohol) Composite-Based Memristor

Yangmin Diao, Bai Sun, et al.

JANUARY 07, 2024

ACS APPLIED MATERIALS & INTERFACES

READ 🗹

Flexible and Freestanding MoS<sub>2</sub>/Graphene Composite for High-Performance Supercapacitors

Chandra Sekhar Bongu, Edreese H. Alsharaeh, et al.

SEPTEMBER 29, 2023

ACS OMEGA

READ 🗹

Integration of a Flexible, Stretchable, Environment-Benign, and Highly Conductive PVA/H<sub>3</sub>PO<sub>4</sub> Hydrogel as a Quasi Solid-State Electrolyte in Reduced Graphene Oxide Supe...

Sangha Mitra and Monica Katiyar

NOVEMBER 21, 2023

ACS APPLIED POLYMER MATERIALS

READ 🗹

**Customizable Resilient Multifunctional Graphene Aerogels** via Blend-spinning assisted Freeze Casting

Yijing Zhao, Wei Zhai, et al.

AUGUST 04, 2023

ACS NANO

READ 🗹

Get More Suggestions >